





Article

Nonuniform Temperature Compensation in Ultrasonic Guided Wave Pipeline Health Monitoring Using Local Phase Matching

Ye Han ¹, Shuo Xia ^{2,*}, Qingchang Wen ¹, Pengfei Zhang ³, Fuzai Lv ^{2,*} and Zhifeng Tang ⁴

¹ Pipe China (Xuzhou) Pipeline Inspection Corporation Limited, Xuzhou 221008, China; hanye02@pipechina.com.cn (Y.H.); 15010383398@163.com (Q.W.)

² School of Mechanical Engineering, Zhejiang University, Hangzhou 310058, China

³ Hangzhou Zheda Jingyi Electromechanical Technology Corporation Limited, Hangzhou 311121, China; zhangpengfei@jingyitech.com

⁴ College of Biomedical Engineering and Instrument Science, Zhejiang University, Hangzhou 310027, China; tangzhifeng@zju.edu.cn

* Correspondence: xsho_arky@zju.edu.cn (S.X.); lfzlfz@zju.edu.cn (F.L.); Tel.: +86-0571-87968239 (F.L.)

Abstract: Faced with a complex working environment, pipelines are prone to nonuniform temperature variations, which cause nonuniform phase changes in the guided wave signals during structural health monitoring, thereby increasing the difficulty of monitoring. To address this, a simulation model is established in this paper to analyze the effects of temperature on material parameters and the variation patterns of guided wave signals. A nonuniform temperature compensation method based on local phase matching is proposed. The algorithm first uses cosine similarity to find the locally best-matched signal segments between the monitoring signal and the baseline signal. Then, an indicator is introduced to quantify the differences between these best-matched signal segments, with the maximum difference considered to be the damage index. Three heating experiments on pipelines with nonuniform temperature fields ranging from 24 °C to 80 °C demonstrate that the proposed method can effectively overcome the resulting phase deviations while achieving high detection accuracy and a reduction false positives. Additionally, the method shows high resolution in detecting defects in both temperature-varying and non-temperature-varying regions.



Citation: Han, Y.; Xia, S.; Wen, Q.; Zhang, P.; Lv, F.; Tang, Z. Nonuniform Temperature Compensation in Ultrasonic Guided Wave Pipeline Health Monitoring Using Local Phase Matching. *Appl. Sci.* **2024**, *14*, 10526. <https://doi.org/10.3390/app142210526>

Academic Editor: Giuseppe Lacidogna

Received: 19 October 2024
Revised: 11 November 2024
Accepted: 13 November 2024
Published: 15 November 2024



Copyright: © 2024 by the authors. Licensee MDPI, Basel, Switzerland. This article is an open access article distributed under the terms and conditions of the Creative Commons Attribution (CC BY) license (<https://creativecommons.org/licenses/by/4.0/>).

Keywords: guided wave monitoring; temperature compensation; defect detection; damage index; local phase matching; signal processing techniques; nonuniform temperature fields

1. Introduction

Pipelines play a vital role in industrial transportation, carrying water, oil, natural gas, chemical products, and more, bringing significant economic value [1]. However, since pipelines are often installed outdoors, they are subjected to complex climate conditions and environmental factors. Exposure to sunlight, nonuniform temperature fluctuations, and stress changes makes them susceptible to damage, such as cracks, corrosion, and deformation [2–5]. As the scale of pipeline transportation expands, these issues become more severe. Therefore, defect detection is crucial to ensure the safety of pipeline operations.

Ultrasonic guided wave (UGW) testing technology offers long detection distances, large coverage areas, full cross-sectional inspection capabilities, and the ability to detect inaccessible regions [6,7], making it especially advantageous for pipeline inspection [8]. Compared to other nondestructive testing methods, such as eddy current testing, magnetic particle inspection, radiographic testing, and ultrasonic bulk wave testing [9–12], guided wave testing offers several advantages. It is easy to operate, highly sensitive, and has a wide detection range. Additionally, it provides reliable results.

Structural health monitoring (SHM) [13–15] can use permanently or semi-permanently fixed transducers to assess structural health and track changes in various indicators remotely and online. It offers high sensitivity and low maintenance costs.

UGW SHM uses signals from the initial healthy state as a baseline to compare with real-time signals, allowing the detection of damage with higher accuracy than traditional UGW testing. However, this method is highly sensitive to temperature changes, which can alter material geometry and properties like the density, Young's modulus, and Poisson's ratio. These changes affect the wave velocity and particle vibration amplitude, leading to variations in the signal travel time. They also cause the stretching, shifting, and attenuation of the received signals. Ultimately, these effects result in false positives and missed detections, impacting monitoring accuracy [16].

For uniform temperature changes, the optimal baseline subtraction (OBS) [17,18] and baseline signal stretch (BSS) [19,20] are the classical temperature compensation methods.

The BSS method primarily uses a global stretching factor to scale the entire signal, thereby compensating for phase changes caused by temperature variations. Building on these, researchers have developed numerous improved methods, such as a combination of OBS and BSS, and various enhanced BSS algorithms [14,18,19,21–23]. With advancements in data and signal processing, algorithms based on orthogonal matching pursuit (OMP) have become widely used in temperature compensation for UGW. Roy et al. [24] developed a method based on matching pursuit (MP) signal analysis and reconstruction schemes. Liu et al. [25] utilized the Hilbert transform to compensate for phase and OMP to compensate for the amplitude of Lamb waves. Fendzi et al. [26] employed the Hilbert transform and the least squares method. Wang et al. [27] considered the influence of both load and temperature changes, proposing a signal compensation technology based on MP.

However, these algorithms either rely on an over-complete signal library or use a single stretching factor, limiting their application to scenarios with uniform temperature changes. In practice, environmental conditions are often complex. When pipelines are shaded by bridges, buildings, vegetation, or hills, uneven sunlight exposure creates nonuniform temperature fields [28]. In such cases, conventional temperature compensation methods struggle to account for the resulting signal variations, significantly restricting their applicability.

Research reports on temperature compensation algorithms for nonuniform variations are relatively limited. Dynamic time warping (DTW) [29,30] algorithms, when compensating for nonuniform temperature changes, are prone to signal overcompensation. This can potentially mask defect information. Additionally, DTW algorithms often require significant computational power, making improvements necessary during implementation [28]. Data-driven compensation algorithms [31], variational autoencoder-based algorithms [32], and neural network-based algorithms [33] are used for nonuniform temperature compensation.

These methods require large amounts of data to mitigate the effects of uneven temperature changes. However, collecting a sufficient variety of signals in practical applications is challenging. This makes these methods difficult to implement in real-world scenarios. In recent years, the rapid development of machine learning and artificial intelligence has significantly advanced UGW monitoring, particularly in the field of temperature compensation [34–37]. However, these methods require substantial computational resources, prior knowledge, and high-quality training samples, which limits their applicability.

Currently, pipeline temperature compensation algorithms typically assume uniform temperature changes across the pipeline. Methods combining OBS and BSS, along with their improved versions, can effectively handle uniform temperature variations. While advanced technologies like OMP, machine learning, and neural networks offer strong compensation capabilities, they require a complete signal database or high-quality learning samples, which are difficult to obtain in practice. The DTW method is time consuming and may obscure defect features. Therefore, there is a need for a convenient, stable, and accurate nonuniform temperature compensation algorithm to meet the UGW monitoring requirements under nonuniform temperature changes.

In addressing nonuniform temperature compensation in pipelines, this paper first establishes a simulation model to analyze the effects of temperature on material properties and UGW signals. It then proposes a new method named local phase matching (LPM).

LPM primarily leverages the local similarity between two signals to perform signal matching, effectively addressing the matching challenges caused by uneven changes throughout the entire signal. Initially, two sliding windows of different sizes divide the baseline signal (BS) and monitoring signal (MS) into various sub-sequences. Subsequently, cosine similarity is employed to locally match these sub-sequences, identifying the most similar local signal sub-sequences. A damage index is then defined to quantitatively assess the matched signal sub-sequences as indicators of defects. To validate the effectiveness of the algorithm, this paper conducts three heating experiments on pipelines under nonuniform temperature fields. These experiments thoroughly assess the temperature compensation capabilities of LPM and its defect detection abilities across different temperature regions. Additionally, a comparison is made with the BSS method.

2. The Effects of Temperature on UGW

Temperature has an impact on the density, Young's modulus, and Poisson's ratio. Q235 steel pipes are commonly used for transporting low-pressure fluids. They are produced in large quantities and have a wide range of applications. According to the Chinese national standards [38], their chemical composition is shown in Table 1.

Table 1. Chemical composition of Q235.

Material Grade	Chemical Composition (Mass Fraction)/%, Not Exceeding				
	C	Si	Mn	P	S
Q235	0.22	0.35	1.40	0.045	0.050

JMatPro, the Java-based Materials Properties software, is a comprehensive simulation tool used to calculate the phase diagrams, physical properties, and thermodynamic properties of metal materials. It includes various built-in modules for materials such as steel, aluminum alloys, magnesium alloys, and titanium alloys. In this paper, JMatPro7.0 is employed to analyze the influence of temperature on the properties of Q235 steel.

The specific material parameters should align with those used in the experiment. Based on the Q235 pipeline manufacturer's test report, the chemical composition is primarily Fe = 98.925%, Mn = 0.55%, Si = 0.26%, C = 0.18%, P = 0.040%, and S = 0.045%. These parameters are input into JMatPro, with the upper temperature limit set to 100 °C and the lower limit to 24 °C. The resulting temperature-dependent property curves are shown in Figure 1.

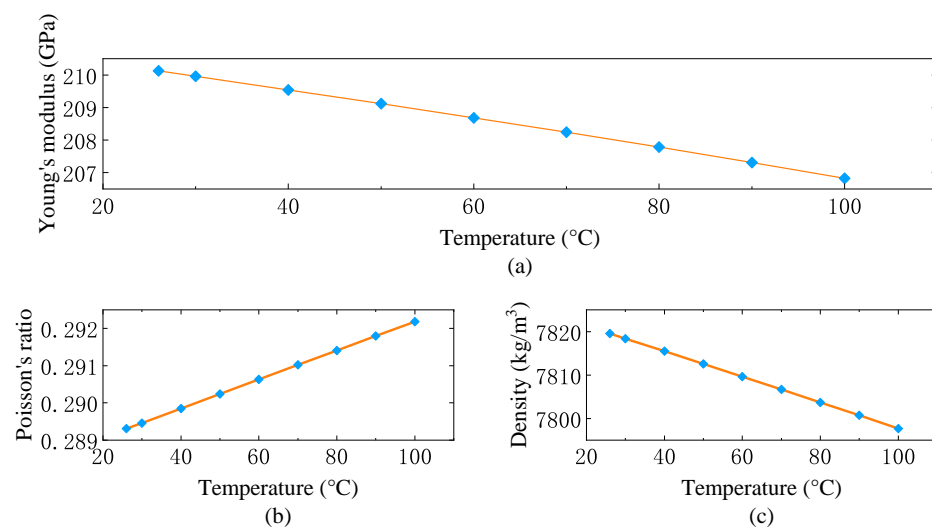


Figure 1. Influence of temperature change on various material properties: (a) Young's modulus; (b) Poisson's ratio; (c) density.

Figure 1 shows the curves of the Young’s modulus, Poisson’s ratio, and density as they vary with temperature. The Young’s modulus and density decrease gradually with increasing temperature, while the Poisson’s ratio increases. It is clear that the effects of temperature on these material properties are linear.

The propagation behavior of guided waves in pipelines is governed by the Navier equations,

$$\mu \nabla^2 \mathbf{u} + (\lambda + \mu) \nabla \nabla \cdot \mathbf{u} = \rho \frac{\partial^2 \mathbf{u}}{\partial t^2}. \tag{1}$$

Considering the boundary conditions of the pipeline,

$$\sigma_{rr} = \sigma_{r\theta} = \sigma_{rz} = 0, \quad r = R_i, \quad r = R_o, \tag{2}$$

it is possible to derive the dispersion characteristic equation of guided waves in the pipeline:

$$\begin{bmatrix} C_{11} & C_{12} & \cdots & C_{16} \\ C_{21} & C_{22} & \cdots & C_{26} \\ \vdots & \vdots & \ddots & \vdots \\ C_{61} & C_{62} & \cdots & C_{66} \end{bmatrix} \begin{bmatrix} A \\ B \\ \vdots \\ B_3 \end{bmatrix} = \begin{bmatrix} 0 \\ 0 \\ \vdots \\ 0 \end{bmatrix}, \tag{3}$$

where C_{ij} is a coefficient matrix of A, B, A_1, B_1, A_3, B_3 . The determinant of the coefficient matrix, $\|C_{ij}\| = 0 (i, j = 1, 2, \dots, 6)$, represents the dispersion equation of guided waves in a free pipe within a vacuum medium [39]. This paper focuses on analyzing the impact of temperature on material properties. As such, only the fully elastic isotropic material model is considered in this analysis.

Due to the inability to obtain an analytical solution for the characteristic equation of guided waves, only numerical solutions can be achieved. Therefore, this paper utilizes COMSOL5.6 simulation software to analyze the propagation behavior of UGW across various temperature fields. The cross-sectional dimensions of the pipeline are consistent with those of the experimental pipeline in this study and conform to the Chinese national standards [40]. The pipe diameter is set to $\phi 219$ mm, with a wall thickness of 6 mm. To minimize simulation time without compromising the analysis, the pipe length is set to 3 m. For the inspection of pipelines, it is optimal to select a mode that is single and exhibits minimal dispersion; thus, the T (0,1) mode, characterized by being single and nondispersive, is the preferred choice. The excitation frequency is set at 128 kHz, with a sine wave excitation modulated by a four-period Hanning window, and the guided wave signal is acquired using a pulse-echo technique. By incorporating the material properties of Q235 into COMSOL, UGW signals under different temperature distributions can be obtained. The simulation is conducted in two steps. First, the effect of uniform temperature changes across the entire pipeline on UGW signal is analyzed. Second, the impact of nonuniform temperature fields on UGW signal is examined. The results are presented in Figure 2.

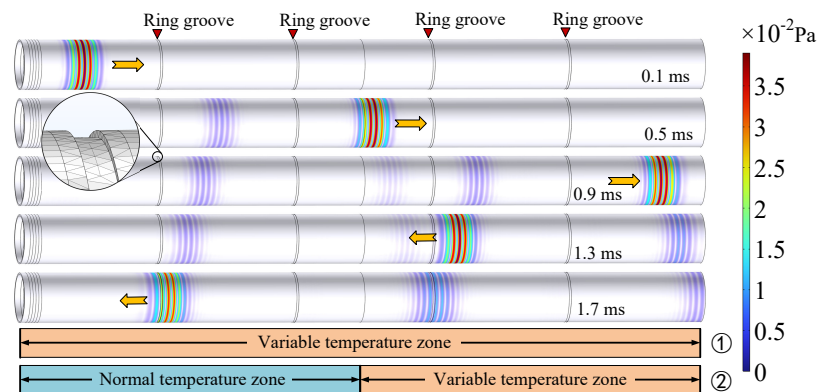


Figure 2. Cloud map of UGW simulation results.

Figure 2 illustrates the cloud map of UGW propagating within the pipeline. The acoustic field in the pipeline is uniform and symmetrical, indicating that the T (0,1) mode is optimally excited. Figure 2 displays the UGW cloud map at propagation times of 0.1 ms, 0.5 ms, 0.9 ms, 1.3 ms, and 1.7 ms. To better analyze phase changes in the guided wave signal during propagation, four annular grooves are incorporated in the pipeline model. These grooves are placed at intervals of 60 cm and serve as signal reference points as shown in Figure 2. Each groove has a width of 4 mm and a depth of 2 mm. During the propagation process, an echo is generated each time the wave passes through an annular groove as depicted by the light-colored cloud image in Figure 2. The simulation is conducted twice, categorizing the temperature changes into a uniform region and a nonuniform region based on their variations. The received signal for the uniform temperature field (UTF) is shown in Figure 3, while the signal corresponding to the nonuniform temperature field (NTF) is presented in Figure 4.

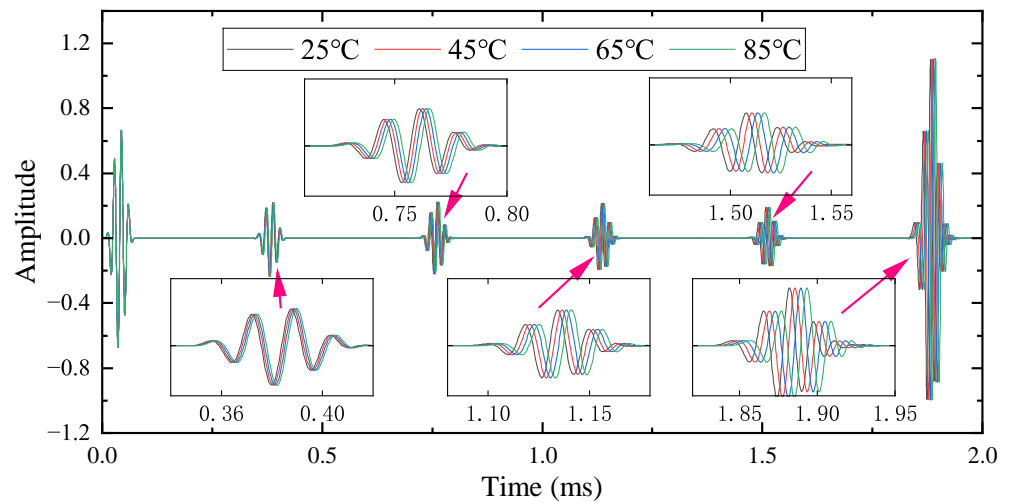


Figure 3. UGW signals at different temperatures during UTF.

Figure 3 illustrates the UGW signals obtained at different temperatures. Due to the uniform nature of the temperature change, its effect on the phase shift is also consistent. As the wave propagates from the first to the fourth annular groove, and subsequently to the end echo, the signal phase shift gradually increases. The influence of the temperature change on the phase can be considered linear, aligning with the findings in the literature [22,25], thereby validating the effectiveness of the simulation results.

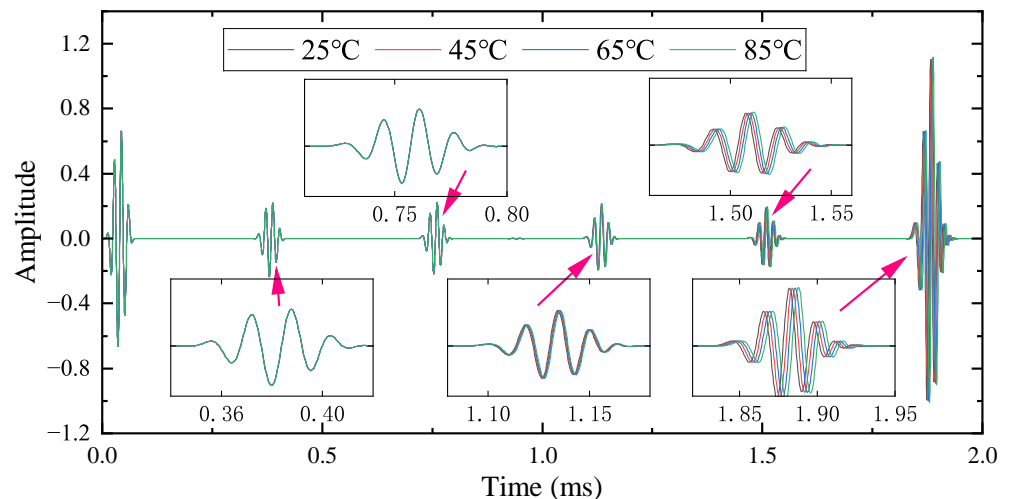


Figure 4. UGW signals at different temperatures during NTF.

The UTF represents an ideal scenario, but in reality, it is often influenced by various complex environmental factors, making the NTF more common. Figure 4 shows the effect of different temperatures on UGW signals under the NTF. In this scenario, one end of the pipeline is at a high temperature, and the other is low. This NTF causes a nonuniform phase shift in signal. The first and second annular grooves are located in the normal temperature region as shown in Figure 2. They are therefore unaffected by temperature changes and show no phase shift. In contrast, the third and fourth annular grooves, along with the pipeline’s end face, are situated in the temperature variation zone. Here, phase delays occur due to the impact of temperature changes. The higher the temperature and the longer the propagation path through the high-temperature region, the greater the phase shift.

Figures 5 and 6 show the phase delay of the UGW signal. The phase delay of the signal in Figure 3 is displayed in Figure 5, with a superimposed fitted line. It can be observed that temperature has a clearly linear influence on the signal phase: the higher the temperature, the greater the phase delay. At the same temperature, the cumulative effect causes the signal phase to exhibit a pronounced linear change as the UGW propagation distance increases.

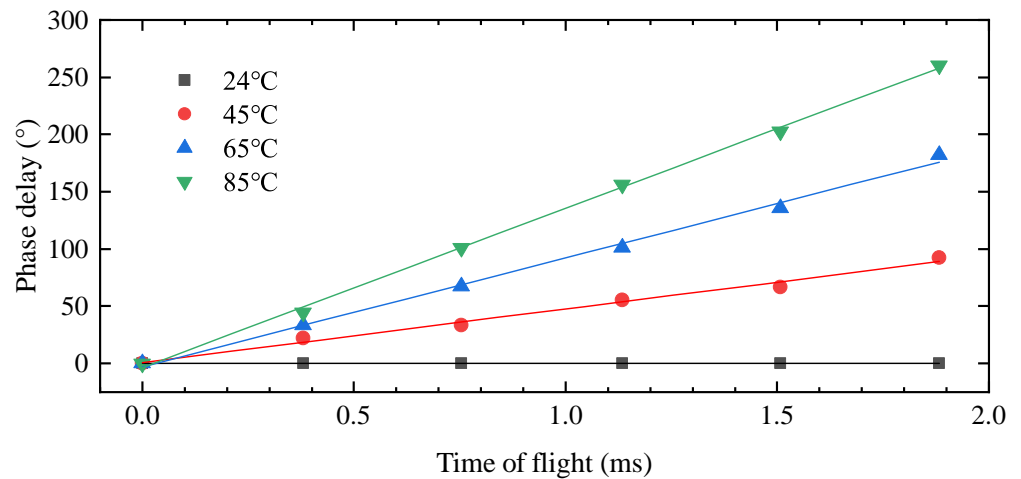


Figure 5. Phase delay at different temperatures for UTF.

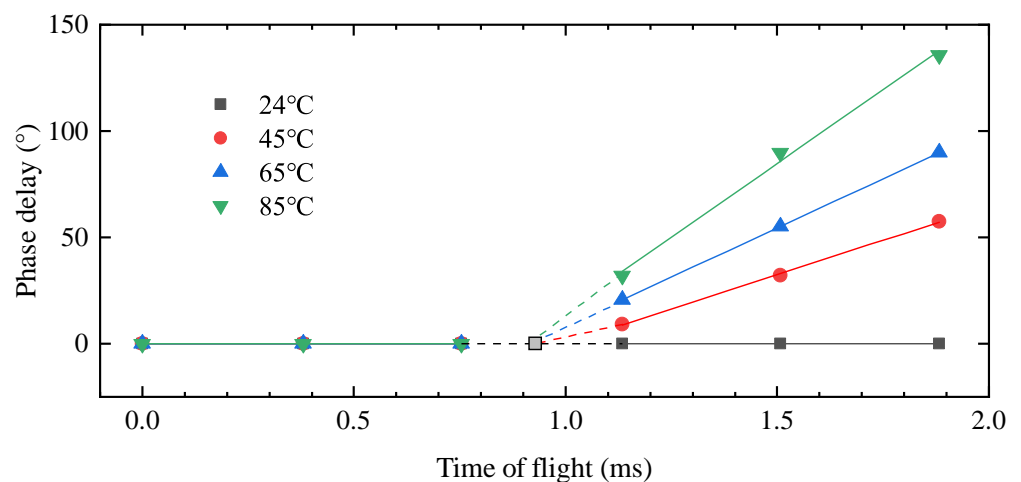


Figure 6. Phase delay at different temperatures for NTF.

Figure 6 illustrates the phase change of the signal in Figure 4. When the UGW propagates under a constant temperature, the phase remains nearly unchanged. However, upon entering a region with varying temperatures, it continues to exhibit a linear trend. In Figure 6, the signal in each temperature range is fitted with straight lines. Due to the

absence of a reference point at the temperature transition junction, reading the signal phase at that point is challenging. Nevertheless, it can be identified by the intersection of the extrapolated fitted lines from either side, which aligns well with the simulated setup. Therefore, temperature variations significantly impact the UGW signal phase, showing a linear relationship.

Consequently, in practical applications, the NTF in pipelines can cause some signals to lead while others lag, introducing interference in UGW monitoring. This highlights the need for an advanced temperature compensation algorithm to overcome these complex temperature variations.

3. Nonuniform Temperature Compensation Using Local Phase Matching

Global signal processing methods often struggle with signals exhibiting nonuniform phase changes due to NTF. Although these signals may lead or lag in phase, they retain a degree of similarity within the local ranges. This paper proposes a method to compensate for the local phase of the signal, effectively addressing the challenges of UGW detection caused by nonuniform phase shifts. Additionally, this algorithm focuses solely on phase compensation. It preserves the original signal information, avoiding the enhancement or masking of defect signals and other characteristics. This broadens its applicability.

In UGW monitoring, health signals from multiple groups of structures in a nondestructive state are first collected as baseline signals (BSs) $B_n = \{b_1, b_2, \dots, b_n\}$. These collected signals, known as monitoring signals (MSs) $Y_n^j = \{y_1, y_2, \dots, y_n\}$ (j -th MS), are then used to assess the structural health.

After obtaining BS and MS, LPM can be performed, with the specific steps outlined as follows:

1. In BS, the width of the baseline sliding window (BSW) is selected as p , and the initial element number of BSW is i . At this point, the elements contained in BSW sequence are as follows:

$$b_p^i = \{b_i, b_{i+1}, \dots, b_{i+p-1}\}; \tag{4}$$

2. In the j -th MS, the width of the monitoring sliding window (MSW) is select as q ($q = p - 2a, a \geq 0$). The initial element number is s ($s = i + a$), and the elements contained in the MSW sequence are as follows:

$$y_q^{js} = \{y_s^j, y_{s+1}^j, \dots, y_{s+q-1}^j\} = \{y_{i+a}^j, y_{i+a+1}^j, \dots, y_{i+p-a-1}^j\}; \tag{5}$$

3. Since the BSW sequence contains $2a$ more elements than the MSW sequence, the BSW sequence can be further divided into $2a + 1$ sub-sequences, expressed as follows:

$$r_q^{ih} = \{b_{i+h}, b_{i+h+1}, \dots, b_{i+h+q-1}\}, (0 \leq h \leq 2a); \tag{6}$$

4. Calculate the cosine similarity C^{ihj} between each of the $2a + 1$ sub-sequences and MSW sequence. This will result in $2a + 1$ sets of values as shown below:

$$C^{ihj} = C^{ihj}(r_q^{ih}, y_q^{js}); \tag{7}$$

5. Find the \hat{h} that maximizes c^{ihj} , indicating that the \hat{h} -th sub-sequence of the BSW sequence is the closest to the MSW sequence. This determines the best-matching baseline local signal $r_q^{\hat{h}}$ and monitoring local signal y_q^{js} :

$$\hat{h} = \arg \max_h \{c^{ihj}\}; \tag{8}$$

6. Computing the local damage index I^i of the two best-matching local signal segments,

$$I^i = I^i(r_q^{\hat{h}}, y_q^{js}); \tag{9}$$

- Slide the window to the next element ($i \rightarrow i + 1$), continuing until all elements in BS have been traversed. Then, the local damage index calculated for each slide window can be organized into a vector:

$$I^j = [I^{j1}, I^{j2}, \dots, I^{jn}]; \tag{10}$$

- The maximum value in the local damage index vector represents the most distinct part of the signal and can be used as the damage index (DI) for MS:

$$DI = \max(I^j). \tag{11}$$

- Then turn to step (1), computing DI of the $(j + 1)$ -th monitoring signal to form a monitoring curve.

The above outlines the main process of the LPM method.

Cosine similarity measures the similarity between two vectors by calculating the cosine of the angle between them. The result depends solely on the direction of the vectors and is independent of their magnitudes. Typically applied in positive space, the cosine similarity yields values between -1 and 1 . Cosine similarity C is primarily used to assess the similarity between two sets of signal segments and to identify the best matching segments. The expression is as follows:

$$C = C(B_n, Y_n) = \frac{\sum_{i=1}^n b_i y_i}{\sqrt{\sum_{i=1}^n b_i b_i} \sqrt{\sum_{i=1}^n y_i y_i}}. \tag{12}$$

The damage index is an indicator used to assess the extent of signal damage, primarily serving to quantify the defect characteristics. A high damage index indicates that the signal has captured defect information, whereas a low index suggests that the system is in a healthy state. The calculation of the local damage index I is given by the following formula:

$$I = I(B_n, Y_n) = \frac{1}{n} \left\| \frac{\sum_{i=1}^n b_i b_i - \sum_{i=1}^n y_i y_i}{\sum_{i=1}^n b_i b_i} \right\| \tag{13}$$

The overall flow of the algorithm is shown in Figure 7.

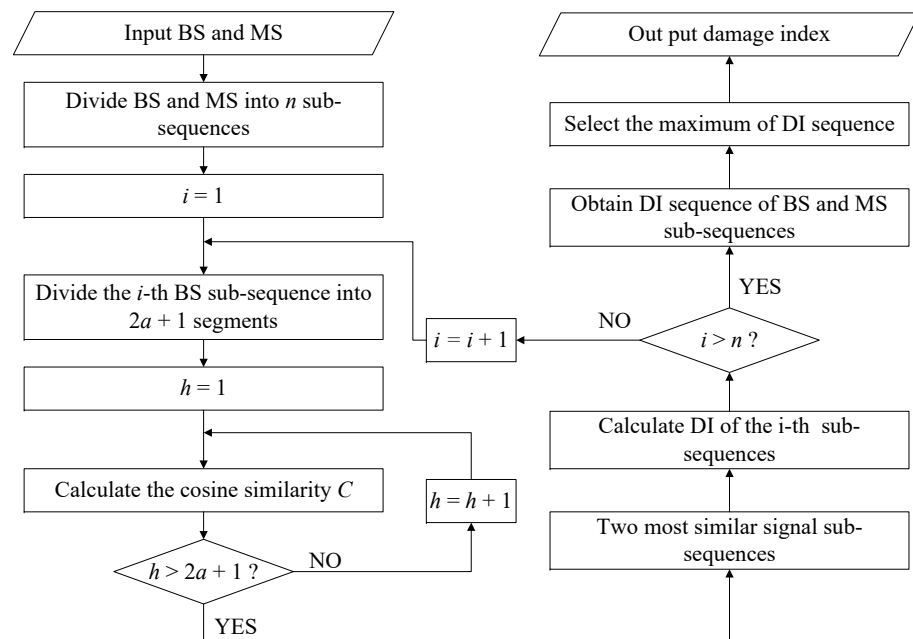


Figure 7. Flowchart of the LPM.

As shown in Figure 7, the main progress involves selecting local signal segments from BS and MS. These segments are then matched using cosine similarity, resulting in two optimally matched groups of local signal segments. Subsequently, DI extracts the differences between these two signals, yielding a value that can be used to assess defects. LPM primarily consists of two cycles, with a fixed number of iterations in each cycle, ensuring low computational complexity suitable for online monitoring.

4. Experimental Setup for Pipeline Heating with NTF

To simulate the potential nonuniform temperature variations that may occur in real-world scenarios and to validate the algorithm, local heating of the pipeline is conducted. The experimental setup is illustrated in Figure 8.

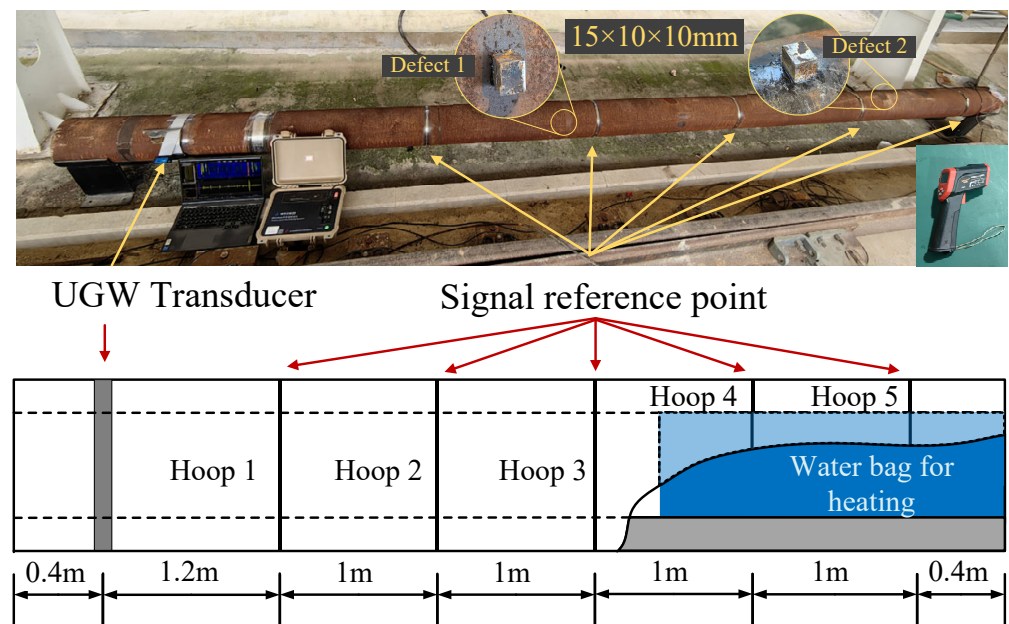


Figure 8. Experimental setup for pipeline heating with NTF.

The experimental pipeline measures 6 m in length, 219 mm in diameter, and 6 mm in thickness. A magnetostrictive patch transducers is positioned 60 cm from one end, with an excitation frequency set to 128 kHz and a sine wave modulated by a four-period Hanning window. UGW monitoring is conducted once per minute during the experiment.

At the opposite end, a water bag is used for heating, creating NTF: one end at normal temperature and the other at high temperature. The water bag is 1.8 m in length. Once filled with water, its outer wall comes into full contact with the inner wall of the pipeline, ensuring efficient heat transfer. This setup divides the pipeline into heating and nonheating areas. After heating, the stable NTF can be categorized into three zones: a low-temperature zone (LTZ) near the unheated end, with temperatures ranging from 24 °C to 30 °C; a high-temperature zone (HTZ) at the heated end, with the temperatures ranging from 78 °C to 83 °C; and a temperature transition zone (TTZ) between them, with temperatures ranging from 30 °C to 78 °C as shown in Figure 9.

As shown in Figure 9, the heating process lasts for 100 min. By the 90th min, the pipeline reached thermal equilibrium, with minimal temperature change over the final 10 min. Therefore, it takes 90 min for the pipeline to be heated from 24 °C to 80 °C at one end, establishing a stable temperature field. In HTZ and LTZ, the surface temperature remains stable and uniform. TTZ experiences sharp temperature changes due to the influences of both adjacent zones, resulting in significant NTF.

Specific operations for the nonuniform heating of the pipeline are as follows: Place the water bag inside the pipeline and fill it with water to ensure full contact with the inner wall. Heat the water from 26 °C to 90 °C; it can maintain the temperature at the end of

the pipeline at a maximum of 80 °C, thus creating an NTF. A temperature measuring gun (shown in Figure 8) can be used to record the temperature change curve of the pipeline at various times and positions, shown in Figure 9.

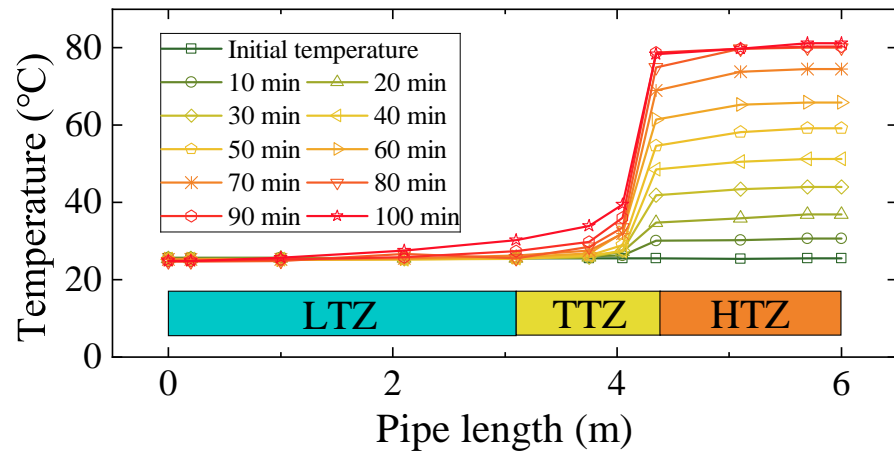


Figure 9. Temperature variation curve at different positions along the pipeline over time.

The temperature change curve of the pipeline over time, shown in Figure 9, indicates that the initial temperature is 24 °C. As heating continued, one end of the pipeline begins to warm up, with UTF occurring in the areas covered by the water bags, while other areas quickly return to normal temperature. After 90 min of heating, the water temperature reaches 90 °C, and the surface temperature of the pipeline stabilizes at 80 °C due to continuous heat dissipation.

To evaluate the phase change in the UGW in pipes with NTF, five metal hoops are installed as reference points for signal phase analysis, shown in Figure 8. Hoop No.1 and No.2 are in LTZ, No.3 is in TTZ, and No.4 and No.5 are in HTZ. The metal hoops are tightly attached to the pipeline surface, generating clear echo signals as shown in Figure 10.

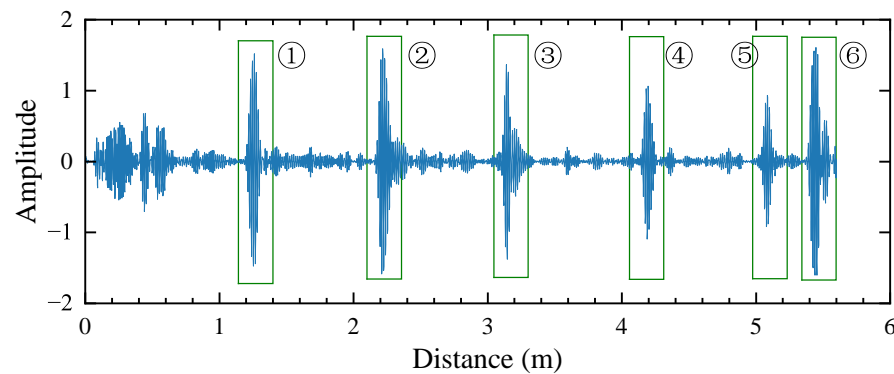


Figure 10. Reflected signal from the pipeline at room temperature (24 °C). No.1 to No.5 are the reflection signals from the metal hoops, and No.6 is the end reflection.

Figure 10 shows the echo signal curve under UTF at room temperature (24 °C). Positions 1 to 5 correspond to the echo signals from five metal hoops, while position 6 indicates the amplitude of the end face. Six echoes are clearly visible. The reflected signal amplitudes from the metal hoops fluctuate and decrease with increasing distance, due to incomplete pre-stressing and guided wave attenuation. In this analysis, the pipeline is considered an ideal elastic body. However, in practice, there is always some energy dissipation. Additionally, with multiple metal hoops present, each guided wave reflects a portion of energy, gradually reducing the energy and, consequently, the signal amplitude. Temperature variations further attenuate the guided waves, impacting the defect identification. Generally, these attenuations are minimal and do not affect the analysis or conclusions of this paper.

To thoroughly investigate the temperature compensation effect and defect detection capability of LPM, three heating experiments are conducted. The first experiment does not include defects and primarily analyzes the signal phase change under an NTF. In the second experiment, defect 1 is introduced in the unheated area to evaluate the algorithm’s defect identification ability in LTZ, locating 2 m from one end of the pipeline. The third experiment involves defect 2 placed in the heated area to assess the algorithm’s performance in HTZ, located 4.4 m from one end of the pipeline. All three heating conditions remain consistent. Due to the high cost of pipeline equipment, simulating defects through drilling or cutting would cause irreparable damage. Thus, it is common practice to simulate defects by attaching iron blocks, each measuring 15 × 10 × 10 mm, shown in Figure 8.

In the second and third heating experiments, heating is initiated only after confirming the receipt of the defect signal echo. Additionally, a specific number of signals are recorded as reference signals before each experiment.

5. Analysis of Experimental Results

5.1. The First Heating Experiment

In the first heating experiment, the signals collected at 24 °C and 80 °C in the pipeline are illustrated in Figure 11. The two signal groups are very similar in shape, with the structural echoes clearly visible. The local details of the signals are presented in Figure 12.

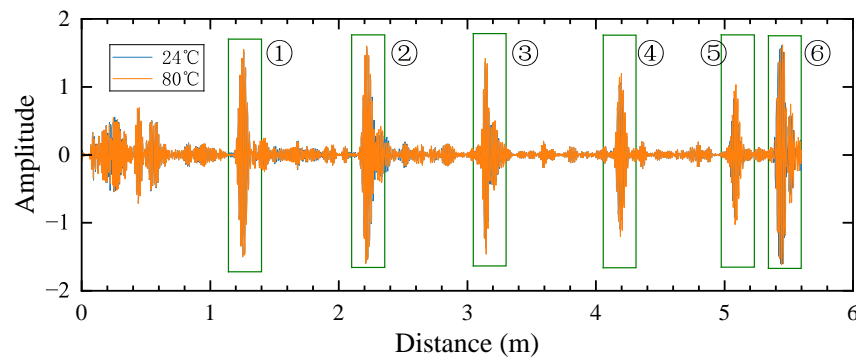


Figure 11. Comparison of the reflecting signals from the pipeline at room temperature (24 °C) and local heating (80 °C). No.1 to No.5 are the reflection signals from the metal hoops, and No.6 is the end reflection.

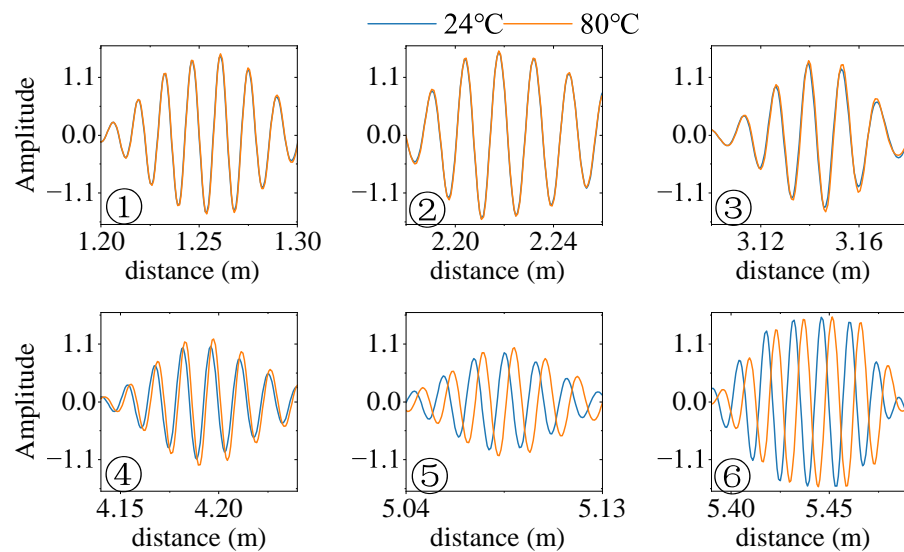


Figure 12. Comparison of the local details of reflected signals before and after locally heated pipelines. No.1 to No.5 are the reflection signals from the metal hoops, and No.6 is the end reflection.

The local phase difference between the high-temperature and low-temperature signals is illustrated in Figure 12. Metal hoops No.1 and No.2 are in LTZ, where the temperature remains nearly constant, resulting in an almost stable phase for UGW signals. Metal hoop No.3, located in TTZ, experiences a slight temperature change, leading to a small phase shift in the UGW signal. In contrast, metal hoops No.4 and No.5, situated in HTZ, exhibit significant temperature variations, causing substantial deviations in the UGW signals. This demonstrates that the temperature has a significant impact on the phase of UGW signals, and as the temperature increases, so does the phase shift. The phase delays for metal hoops No.1 to No.3 are all 0° , while those for metal hoops No.4 to No.6 are 20.0° , 120.0° , and 139.9° , respectively. Although these values differ slightly from the simulation results, the variations are within an acceptable error range when accounting for differences in the lengths of experimental pipes and other practical factors. It confirms the success of the experiment.

5.1.1. Analysis of Experimental Results Using BSS

This section analyzes the compensation effect of the BSS method. As shown in the reference [21], the BSS method minimizes the average residual between the stretched baseline and monitoring signals through a global stretching factor, thus achieving temperature compensation. This can be described by the following formula:

$$\hat{\beta}_{ms} = \arg \min_{\beta} \{R\}, \quad (14)$$

$$R = \int_{t_1}^{t_2} [u(t, T) - \hat{u}(t, T_0, \hat{\beta})]^2 dt, \quad (15)$$

where $\hat{\beta}_{ms}$ represents the optimal stretching factor, and T_0 and T denote the signals at the initial and current temperatures, respectively. \hat{u} is the baseline signal after stretching, and R represents the mean square error between the two signals. This error serves as a measure of signal disparity and can be used as a damage index.

Figure 13 shows the local phase diagram of the signals after compensation using the BSS. The BSS signal at position 1 (metal hoop 1) exhibits a slight phase lag compared to the high-temperature signal, while the BSS signal at position 2 (metal hoop 2) shows a greater degree of phase lag. The BSS signals at positions 3 and 4 (metal hoops 3 and 4) have similar phase lag levels. However, due to the inherent phase lag of signals in the temperature transition and high-temperature zones, the phase lag at positions 3 and 4 tends to decrease. The BSS phase at position 5 (metal hoop 5) is comparable to the high-temperature signal. Position 6 represents the end face signal, where the BSS processing results in a phase advancement compared to the test signal. Throughout the BSS processing, while some signals (e.g., at position 5) align well, most signals exhibit either a phase advancement (position 6) or a lag (positions 1, 2, 3, and 4).

BSS applies a single stretching factor to transform signals, which is effective for uniform phase changes as already demonstrated. However, for signals with nonuniform phase changes—where some phases remain unchanged while others vary—the compensation effect of BSS is limited. This results in excessive compensation for the phase of signals in the nontemperature-variable region, while the phase compensation for signals in temperature-variable areas is insufficient.

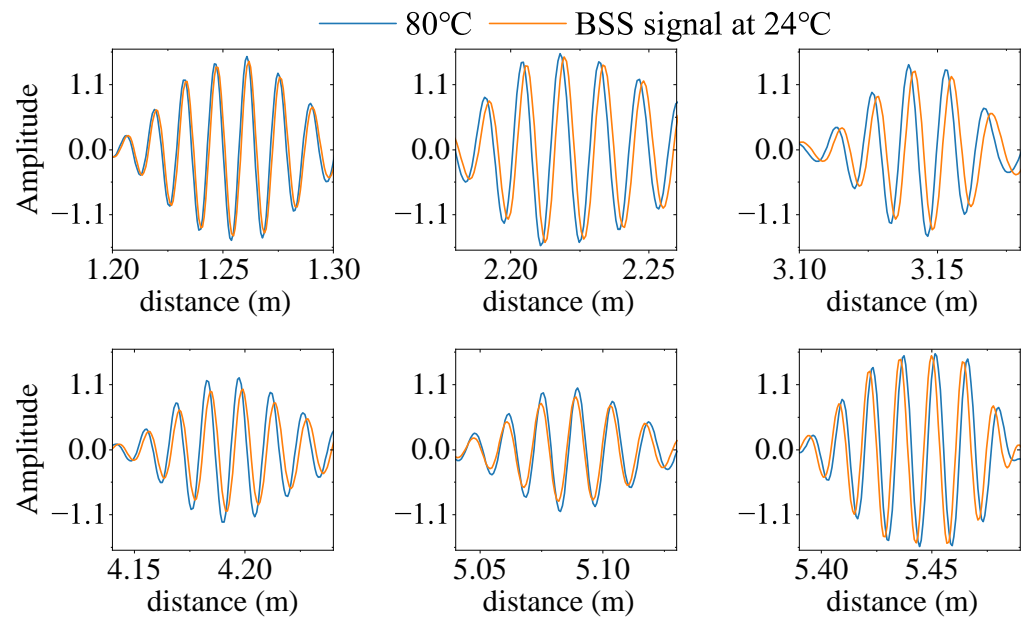


Figure 13. Local view of signal phase after compensation using the BSS method.

5.1.2. Analysis of Experimental Results Using LPM

The local phase of the compensated variable temperature signal using the proposed LPM method is shown in Figure 14.

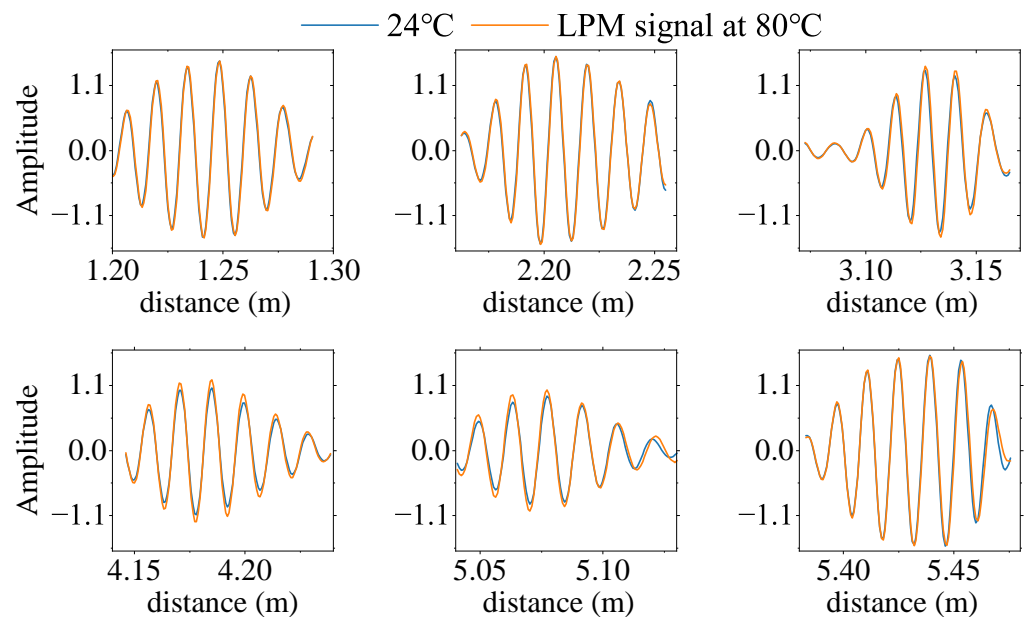


Figure 14. Local view of signal phase after compensation using the LPM method.

In Figure 14, it can be seen that the signal phases at positions 1 and 2 align perfectly, consistent with the phase conditions of the original signals at 24 °C, and there is no sign of overcompensation observed in Figure 13. The metal hoop at position 3 is in TTZ, where the temperature experiences slight variations, and the LPM method effectively compensates for the phase, showing improved matching compared to Figures 12 and 13. Positions 4, 5, and 6 are all in the HTZ, where phase variations are significant. The LPM method provides effective phase compensation, bringing the compensated phase very close to that of BS at 24 °C. This demonstrates that LPM can accurately match the local phases of signals, making

it suitable for signals with nonuniform phase changes, thus offering enhanced stability and a broader range of applications.

5.1.3. Damage Index Curves for Two Methods

Further investigation into the changes in DI for the two methods used to quantify defects is presented in Figure 15.

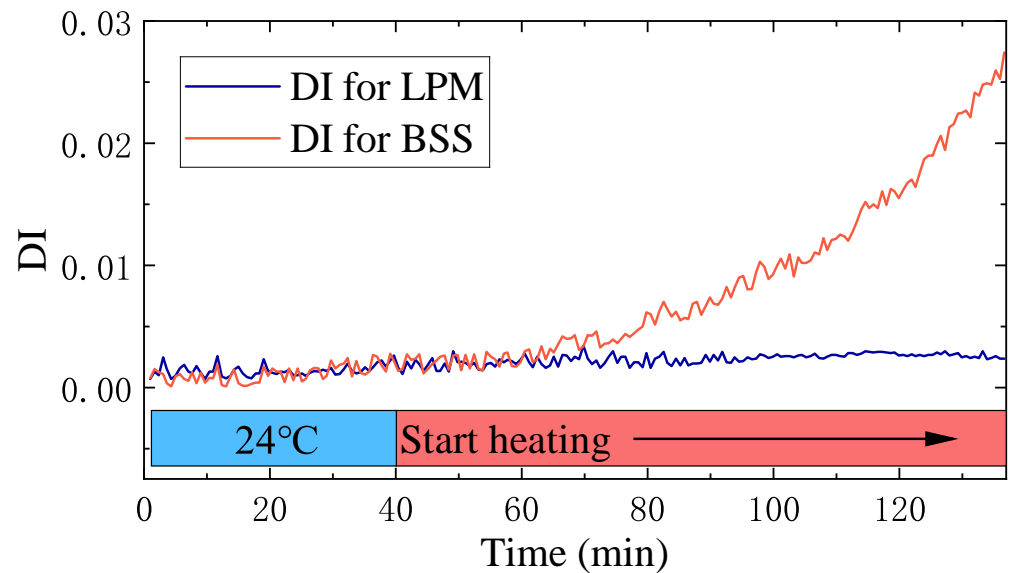


Figure 15. Variation curves of damage index for BSS method and LPM method with time.

Figure 15 illustrates the trends of DI for both the BSS method and the LPM method over time. Initially, signals are collected at a normal temperature for a period. At the 40th minute, the pipeline is heated, and after approximately 90 min of heating, the system reaches its highest temperature.

As shown in Figure 15, DI for BSS remains between 0 and 0.0027, and the DI for LPM stays between 0 and 0.0025. Both damage indices are very low, indicating a healthy system with no defects. However, as the pipeline temperature changes unevenly, DI for BSS begins to increase significantly, with the maximum value reaching 0.027. This rise is attributed to the method's incomplete phase compensation for the NTF, suggesting potential defects in the system. Nevertheless, this increase may lead to false positives.

In contrast, DI for LPM remains relatively stable, indicating that NTFs do not affect its accuracy. This demonstrates the LPM method's effective temperature compensation capabilities.

5.2. The Defect Is Located in the Unheated Area

The second heating experiment aims to assess the algorithm's ability to detect pipeline defects in LTZ. First, a defect-free signal of the pipeline at room temperature is collected over a period. Then, an iron block measuring $15 \times 10 \times 10$ mm is attached 2 m from one end of the pipeline as indicated by Defect 1 in Figure 8. The collected signal during this phase is shown in Figure 16.

Figure 16 displays the reflected signal of the pipeline containing defects at room temperature. An echo is clearly visible at 2 m, corresponding to the position of the iron block. Afterward, one end of the pipeline is heated, completing the process after approximately 90 min, with the outer surface reaching 80 °C. DI curves for the LPM and BSS methods over time are illustrated in Figure 17.

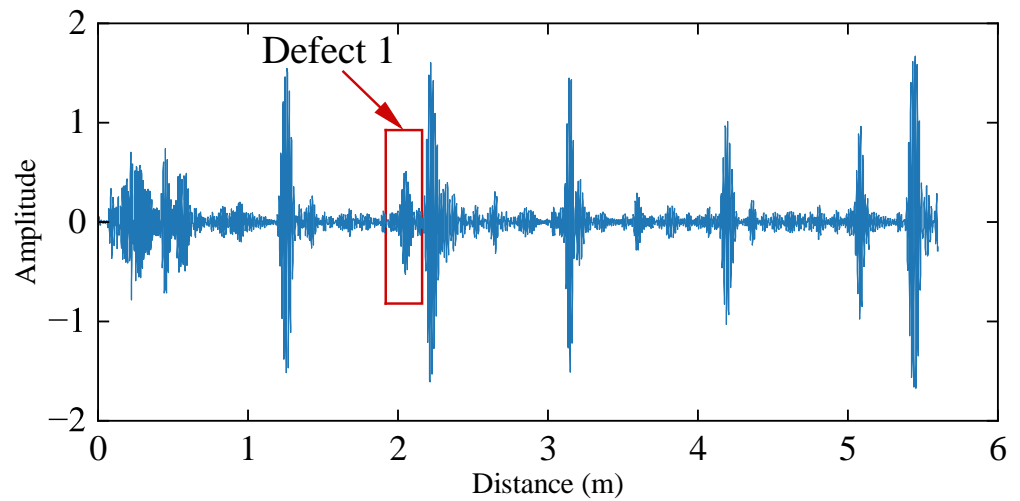


Figure 16. The reflected signal of Defect 1 in pipeline at 24 °C.

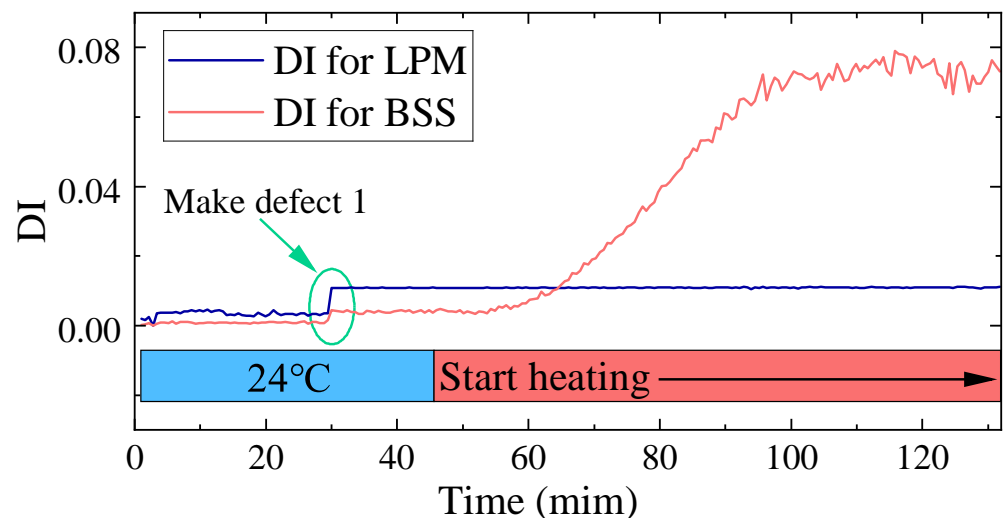


Figure 17. Variation curves of damage index for the BSS method and LPM method over time with the defect located in the unheated area.

Figure 17 shows that the DI curves calculated by both methods remain low and stable when the pipeline is defect-free at room temperature. The defect is introduced at the 30th minute, resulting in a noticeable step change in both curves, indicating that both algorithms effectively detect defects at room temperature. After 45 min, heating begins at one end of the pipeline. Following this, the DI of the BSS method increases continuously, eventually reflecting that the influence of the temperature change surpasses that of the defect. This could lead to missed detection in the pipeline with an NTF. In contrast, the DI for the LPM method remains stable despite the rising temperature, showing minimal sensitivity to temperature changes.

This experiment demonstrates that the LPM method effectively mitigates the impact of NTF in pipelines and maintains strong detection capabilities for defects in LTZ.

5.3. The Defect Is Located in the Heated Area

To evaluate the ability of the LPM method to detect defects in the HTZ, this paper conducts the third heating experiment. Initially, the echo signal of the pipeline in a healthy state is collected. After a period of time, an iron block is attached at a position 4.4 m from one end of the pipeline as indicated in Defect 2 in Figure 6. The process and settings for attaching the iron block are identical to those in the second experiment. The signals collected after the attachment, which include defects, are shown in Figure 18.

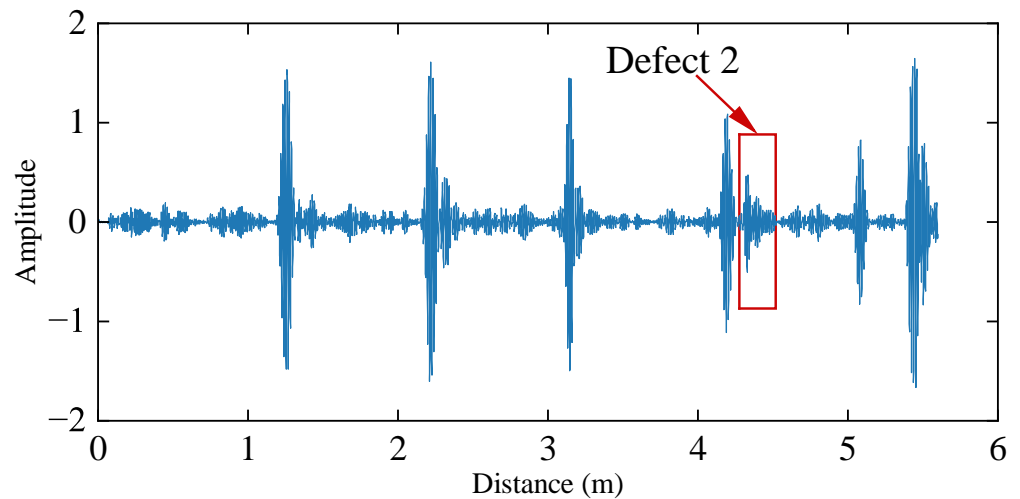


Figure 18. The reflected signal of Defect 2 in pipeline at 24 °C.

Figure 18 shows the reflected signal after the iron block is attached in the HTZ at 24 °C. At 4.4 m, a clear echo can be observed, confirming the effectiveness of the iron block in simulating defect. Subsequently, one end of the pipeline is heated to create an NTF. After 90 min of heating, the temperature at that end reaches a maximum of 80 °C. The DI curves over time for both methods are calculated and presented in Figure 19.

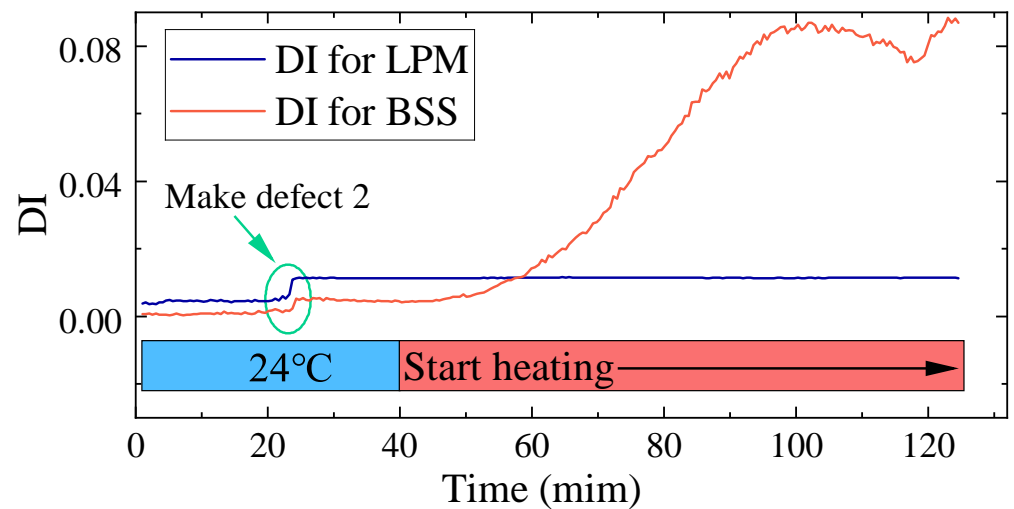


Figure 19. Variation curves of damage index for the BSS method and LPM method over time with the defect located in the heated area.

Figure 19 shows the DI curves over time for the BSS and LPM methods. During the first 23 min of the experiment, the damage indexes for both algorithms remain stable within a small range. At the 23th minute, the iron block is attached, resulting in a noticeable step change in both indexes, which persists for 15 min until heating commences. When the experiment reaches 38 min, the DI of the BSS method sharply increases with the rising temperature. In contrast, the DI of the LPM method remains relatively stable after heating, effectively mitigating the impact of the NTF.

The third heating experiment demonstrates that the LPM method can successfully detect defects in the high-temperature area of a pipeline under an NTF.

5.4. Discussion on LPM

LPM demonstrates strong temperature compensation performance across different temperature regions, such as TTZ and HTZ. This is because LPM divides MS into multiple

signal sub-sequences, allowing each to be locally matched with nearby BS. Cosine similarity effectively measures these local similarities, enabling the LPM to accurately match the phases despite a certain phase delay. Under the influence of an NTF, the local phase of the signal may lag or lead, but this change is localized. Therefore, precise phase information can be obtained by matching each local change, effectively overcoming temperature-induced phase variations.

However, LPM primarily relies on calculating the local similarity between two signals sequentially for phase matching. When the temperature is too high, the signal phase delay increases significantly, requiring a broader local range to capture these changes. This can lead to incorrect matches and false positives during local matching.

Since LPM is a signal processing technique, it can be applied across various pipeline materials and environments. For complex environments or structures, an appropriate signal excitation and reception system should be in place. Once a stable UGW signal is collected, LPM can be used to compensate for temperature variations. Consequently, the LPM method has broad applicability.

6. Conclusions

This paper proposes a signal phase local matching method for temperature compensation and UGW monitoring in pipelines experiencing NTF, which often occur in real-world scenarios. The influence of temperature on material properties is analyzed using simulation software, followed by the establishment of a three-dimensional simulation to further examine how temperature affects UGW signals. Three heating experiments with NTF are conducted to validate the method's effectiveness in temperature compensation and defect detection, comparing its performance with the BSS method. The main conclusions are as follows:

The impact of temperature changes on the material parameters is nearly linear. The Young's modulus and density decrease with increasing temperature, while the Poisson's ratio increases. These variations in the material properties lead to phase shifts in the UGW signals, resulting in nonuniform phase shifts under an NTF.

In an NTF, the BSS method employs a global stretching factor, which can cause overcompensation in the nonvariable temperature regions while undercompensating in variable temperature regions, making practical application challenging. Conversely, the proposed LPM method effectively calculates the cosine similarity of local signal segments, allowing for precise phase matching and overcoming the uneven phase changes caused by temperature fluctuations. A method for calculating a damage index is also proposed to assess defect.

By utilizing local phase matching and an efficient damage index, LPM achieves strong temperature stability and high detection accuracy.

The three heating experiments demonstrate that LPM provides excellent resolution for detecting defects in both high and low-temperature areas within an NTF ranging from 24 °C to 80 °C, being almost unaffected by temperature changes. Consequently, it exhibits good temperature stability and a broader range of practical applications.

In future work, we will test LPM on other materials and in real-world conditions to further validate its ability.

Author Contributions: Conceptualization, Y.H. and F.L.; methodology, S.X.; software, P.Z.; validation, S.X., P.Z. and Z.T.; formal analysis, Q.W.; investigation, S.X.; writing—original draft preparation, S.X.; writing—review and editing, Y.H.; visualization, Q.W.; supervision, Q.W.; project administration, P.Z.; funding acquisition, Y.H., F.L. and Z.T. All authors have read and agreed to the published version of the manuscript.

Funding: This research was funded by National Key R&D Program of China under Grant (2023YFF0716600), and Research on the Deep Application of Large Storage Tank Integrity Management (AQWH202208).

Data Availability Statement: The original contributions presented in the study are included in the article, further inquiries can be directed to the corresponding authors.

Conflicts of Interest: Authors Ye Han and Qingchang Wen were employed by the company Pipe China (Xuzhou) Pipeline Inspection Corporation Limited. Author Pengfei Zhang was employed by the company Hangzhou Zheda Jingyi Electromechanical Technology Corporation Limited. The remaining authors declare that the research was conducted in the absence of any commercial or financial relationships that could be construed as a potential conflict of interest.

Abbreviations

The following abbreviations are used in this manuscript:

UGW	Ultrasonic Guided Wave
SHM	Structural Health Monitoring
BSS	Baseline Signal Stretch
LPM	Local Phase Matching
UTF	Uniform Temperature Field
NTF	Nonuniform Temperature Field
BS	Baseline Signals
MS	Monitoring Signals
BSW	Baseline Sliding Window
MSW	Monitoring Sliding Window
DI	Damage Index
LTZ	Low-Temperature Zone
HTZ	High-Temperature Zone
TTZ	Temperature Transition Zone

References

- Gao, Z.; Gong, B.; Xu, Q.; Wang, D.; Deng, C.; Yu, Y. High cycle fatigue behaviors of API X65 pipeline steel welded joints in air and H₂S solution environment. *Int. J. Hydrogen Energy* **2021**, *46*, 10423–10437. [[CrossRef](#)]
- Nguyen, T.T.; Heo, H.M.; Park, J.; Nahm, S.H.; Beak, U.B. Fracture properties and fatigue life assessment of API X70 pipeline steel under the effect of an environment containing hydrogen. *J. Mech. Sci. Technol.* **2021**, *35*, 1445–1455. [[CrossRef](#)]
- Shahriar, A.; Sadiq, R.; Tesfamariam, S. Risk analysis for oil & gas pipelines: A sustainability assessment approach using fuzzy based bow-tie analysis. *J. Loss Prev. Process Ind.* **2012**, *25*, 505–523.
- Vairo, T.; Magri, S.; Qualgliati, M.; Reverberi, A.P.; Fabiano, B. An oil pipeline catastrophic failure: Accident scenario modelling and emergency response development. *Chem. Eng. Trans.* **2017**, *57*, 373–378.
- Ni, P.; Mangalathu, S. Fragility analysis of gray iron pipelines subjected to tunneling induced ground settlement. *Tunn. Undergr. Space Technol.* **2018**, *76*, 133–144. [[CrossRef](#)]
- Zang, X.; Xu, Z.D.; Lu, H.; Zhu, C.; Zhang, Z. Ultrasonic guided wave techniques and applications in pipeline defect detection: A review. *Int. J. Press. Vessel. Pip.* **2023**, *206*, 105033. [[CrossRef](#)]
- Ling, E.H.; Abdul Rahim, R.H. A review on ultrasonic guided wave technology. *Aust. J. Mech. Eng.* **2020**, *18*, 32–44. [[CrossRef](#)]
- Yeung, C.; Ng, C.T. Nonlinear guided wave mixing in pipes for detection of material nonlinearity. *J. Sound Vib.* **2020**, *485*, 115541. [[CrossRef](#)]
- Rifai, D.; Abdalla, A.N.; Razali, R.; Ali, K.; Faraj, M.A. An eddy current testing platform system for pipe defect inspection based on an optimized eddy current technique probe design. *Sensors* **2017**, *17*, 579. [[CrossRef](#)]
- Silva, W.; Lopes, R.; Zscherpel, U.; Meinel, D.; Ewert, U. X-ray imaging techniques for inspection of composite pipelines. *Micron* **2021**, *145*, 103033. [[CrossRef](#)]
- Cai, X.; Chen, Y.; Ma, H.; Qiu, G.; Kang, Y. Visual inspection method of steel pipe surface cracks based on dry magnetic particle feature enhancement. *Nondestruct. Test. Eval.* **2023**, *38*, 254–274. [[CrossRef](#)]
- Shi, Y.; Zhang, C.; Li, R.; Cai, M.; Jia, G. Theory and application of magnetic flux leakage pipeline detection. *Sensors* **2015**, *15*, 31036–31055. [[CrossRef](#)] [[PubMed](#)]
- Yan, F.; Royer Jr, R.L.; Rose, J.L. Ultrasonic guided wave imaging techniques in structural health monitoring. *J. Intell. Mater. Syst. Struct.* **2010**, *21*, 377–384. [[CrossRef](#)]
- Salmanpour, M.; Sharif Khodaei, Z.; Aliabadi, M. Guided wave temperature correction methods in structural health monitoring. *J. Intell. Mater. Syst. Struct.* **2017**, *28*, 604–618. [[CrossRef](#)]
- Mitra, M.; Gopalakrishnan, S. Guided wave based structural health monitoring: A review. *Smart Mater. Struct.* **2016**, *25*, 053001. [[CrossRef](#)]
- Li, D.; Shi, M.; Xu, F.; Liu, C.; Zhang, J.; Ta, D. A new approach to guided wave ray tomography for temperature-robust damage detection using piezoelectric sensors. *Sensors* **2018**, *18*, 3518. [[CrossRef](#)] [[PubMed](#)]
- Konstantinidis, G.; Drinkwater, B.W.; Wilcox, P.D. The temperature stability of guided wave structural health monitoring systems. *Smart Mater. Struct.* **2006**, *15*, 967. [[CrossRef](#)]

18. Clarke, T.; Simonetti, F.; Cawley, P. Guided wave health monitoring of complex structures by sparse array systems: Influence of temperature changes on performance. *J. Sound Vib.* **2010**, *329*, 2306–2322. [[CrossRef](#)]
19. Lu, Y.; Michaels, J.E. A methodology for structural health monitoring with diffuse ultrasonic waves in the presence of temperature variations. *Ultrasonics* **2005**, *43*, 717–731. [[CrossRef](#)]
20. Croxford, A.J.; Wilcox, P.D.; Konstantinidis, G.; Drinkwater, B.W. Strategies for overcoming the effect of temperature on guided wave structural health monitoring. In Proceedings of the Health Monitoring of Structural and Biological Systems 2007, San Diego, CA, USA, 19–22 March 2007; Volume 6532, pp. 590–599.
21. Croxford, A.J.; Moll, J.; Wilcox, P.D.; Michaels, J.E. Efficient temperature compensation strategies for guided wave structural health monitoring. *Ultrasonics* **2010**, *50*, 517–528. [[CrossRef](#)]
22. Wang, Y.; Gao, L.; Yuan, S.; Qiu, L.; Qing, X. An adaptive filter-based temperature compensation technique for structural health monitoring. *J. Intell. Mater. Syst. Struct.* **2014**, *25*, 2187–2198. [[CrossRef](#)]
23. Mariani, S.; Heinlein, S.; Cawley, P. Compensation for temperature-dependent phase and velocity of guided wave signals in baseline subtraction for structural health monitoring. *Struct. Health Monit.* **2020**, *19*, 26–47. [[CrossRef](#)]
24. Roy, S.; Lonkar, K.; Janapati, V.; Chang, F.K. A novel physics-based temperature compensation model for structural health monitoring using ultrasonic guided waves. *Struct. Health Monit.* **2014**, *13*, 321–342. [[CrossRef](#)]
25. Liu, G.; Xiao, Y.; Zhang, H.; Ren, G. Baseline signal reconstruction for temperature compensation in lamb wave-based damage detection. *Sensors* **2016**, *16*, 1273. [[CrossRef](#)] [[PubMed](#)]
26. Fendzi, C.; Rebillat, M.; Mechbal, N.; Guskov, M.; Coffignal, G. A data-driven temperature compensation approach for Structural Health Monitoring using Lamb waves. *Struct. Health Monit.* **2016**, *15*, 525–540. [[CrossRef](#)]
27. Wang, Y.; Wang, G.; Wu, D.; Wang, Y.; Miao, B.; Sun, H.; Qing, X. An improved matching pursuit-based temperature and load compensation method for ultrasonic guided wave signals. *IEEE Access* **2020**, *8*, 67530–67541. [[CrossRef](#)]
28. Cai, J.; Fei, W.; Fu, S.; Lu, M.; Yang, H. High reliability damage imaging under non-uniform environmental temperature variations based on modified dynamic time warping. *Mech. Syst. Signal Process.* **2023**, *203*, 110737. [[CrossRef](#)]
29. Douglass, A.; Harley, J.B. Dynamic time warping for temperature compensation in structural health monitoring. In *Proceedings of the AIP Conference Proceedings*; AIP Publishing: College Park, MD, USA, 2017; Volume 1806.
30. Douglass, A.C.S.; Harley, J.B. Dynamic Time Warping Temperature Compensation for Guided Wave Structural Health Monitoring. *IEEE Trans. Ultrason. Ferroelectr. Freq. Control* **2018**, *65*, 851–861. [[CrossRef](#)]
31. Sun, H.; Yi, J.; Xu, Y.; Wang, Y.; Qing, X. Identification and compensation technique of ure temperature field for Lamb wave-and multiple sensors-based damage detection. *Sensors* **2019**, *19*, 2930. [[CrossRef](#)]
32. Khurjekar, I.D.; Harley, J.B. Closing the sim-to-real gap in guided wave damage detection with adversarial training of variational auto-encoders. In Proceedings of the ICASSP 2022-2022 IEEE International Conference on Acoustics, Speech and Signal Processing (ICASSP), Virtual, 7–13 May 2022; pp. 3823–3827.
33. Sawant, S.; Patil, S.; Thalapil, J.; Banerjee, S.; Tallur, S. Temperature variation compensated damage classification and localisation in ultrasonic guided wave SHM using self-learnt features and Gaussian mixture models. *Smart Mater. Struct.* **2022**, *31*, 055008. [[CrossRef](#)]
34. Yan, A.M.; Kerschen, G.; De Boe, P.; Golinval, J.C. Structural damage diagnosis under varying environmental conditions—Part I: A linear analysis. *Mech. Syst. Signal Process.* **2005**, *19*, 847–864. [[CrossRef](#)]
35. Moll, J.; Kexel, C.; Pöttsch, S.; Rennoch, M.; Herrmann, A.S. Temperature affected guided wave propagation in a composite plate complementing the Open Guided Waves Platform. *Sci. Data* **2019**, *6*, 191. [[CrossRef](#)] [[PubMed](#)]
36. Wang, P.; Zhou, W.; Bao, Y.; Li, H. Ice monitoring of a full-scale wind turbine blade using ultrasonic guided waves under varying temperature conditions. *Struct. Control Health Monit.* **2018**, *25*, e2138. [[CrossRef](#)]
37. Du, F.; Wu, S.; Xing, S.; Xu, C.; Su, Z. Temperature compensation to guided wave-based monitoring of bolt loosening using an attention-based multi-task network. *Struct. Health Monit.* **2023**, *22*, 1893–1910. [[CrossRef](#)]
38. *GB/T 700-2006*; Carbon Structural Steels. Standardization Administration of China: Beijing, China, 2006.
39. Bartoli, I.; Marzani, A.; Di Scalea, F.L.; Viola, E. Modeling wave propagation in damped waveguides of arbitrary cross-section. *J. Sound Vib.* **2006**, *295*, 685–707. [[CrossRef](#)]
40. *GB/T 17395-2008*; General Rules for Steel Pipe Design. Standardization Administration of China: Beijing, China, 2008.

Disclaimer/Publisher’s Note: The statements, opinions and data contained in all publications are solely those of the individual author(s) and contributor(s) and not of MDPI and/or the editor(s). MDPI and/or the editor(s) disclaim responsibility for any injury to people or property resulting from any ideas, methods, instructions or products referred to in the content.